Supporting Information for

Efficient Electrosynthesis of Hydrogen Peroxide in Neutral Media using Boron and Nitrogen Doped Carbon Catalysts

Brianna N. Ruggiero[1], *Xiao Kun Lu*[1], *Bingzhang Lu*[1], *Adrien E. Deberghes*[1], *Dennis Nordlund*[2], *Justin M. Notestein*[1], *Linsey C. Seitz*[1]*

[1]Department of Chemical and Biological Engineering, Northwestern University, Evanston, Illinois 60208-3113, United States

[2]SLAC National Accelerator Laboratory, 2575 Sand Hill Rd, Menlo Park, California, 94025, United States

***Corresponding Author**:
linsey.seitz@northwestern.edu

Table of Contents

Section S1. Methods and Reactor Designs

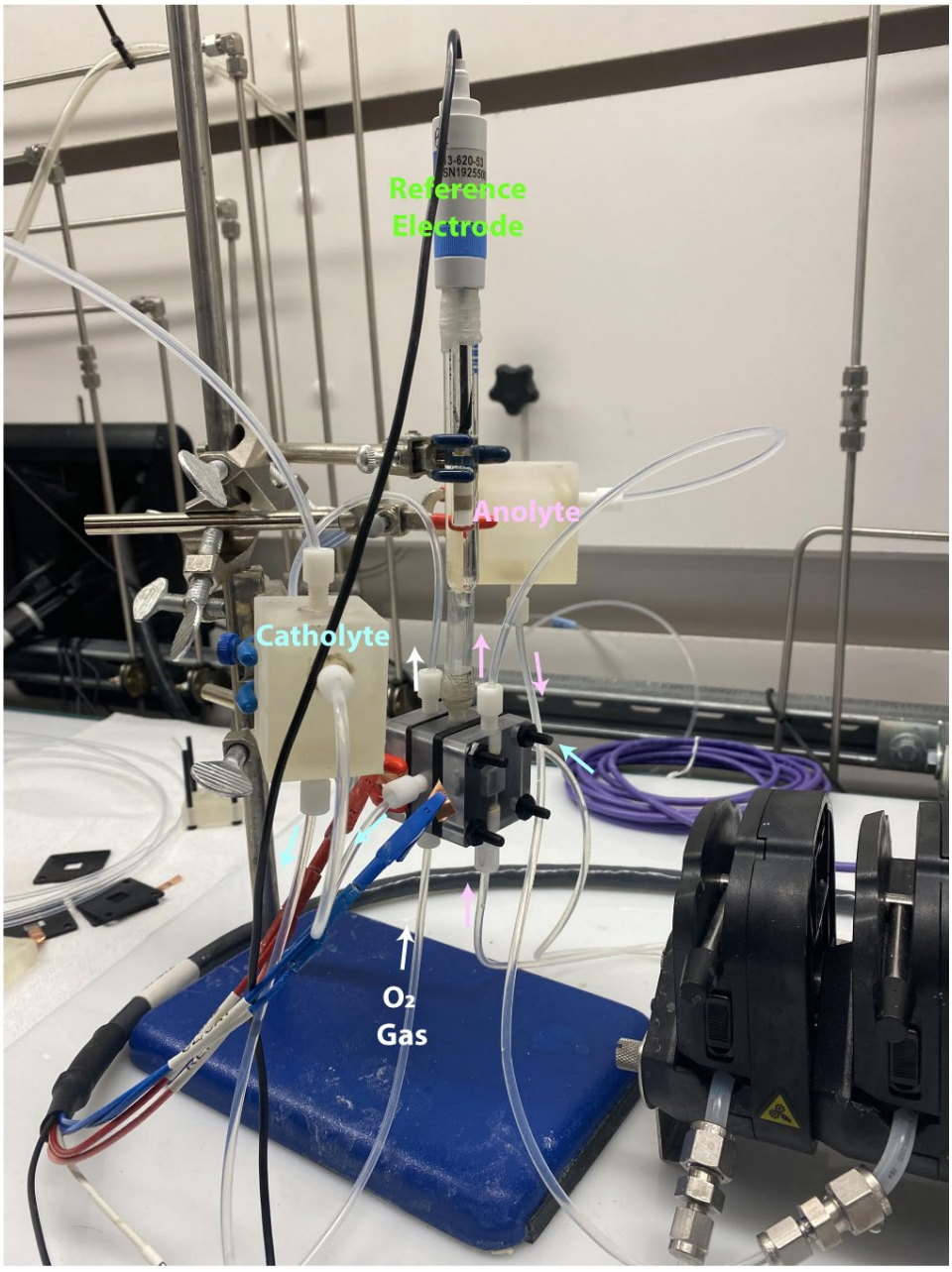

Figure S1. Demonstration of three-electrode gas diffusion electrode (GDE) electrochemical flow cell set-up.

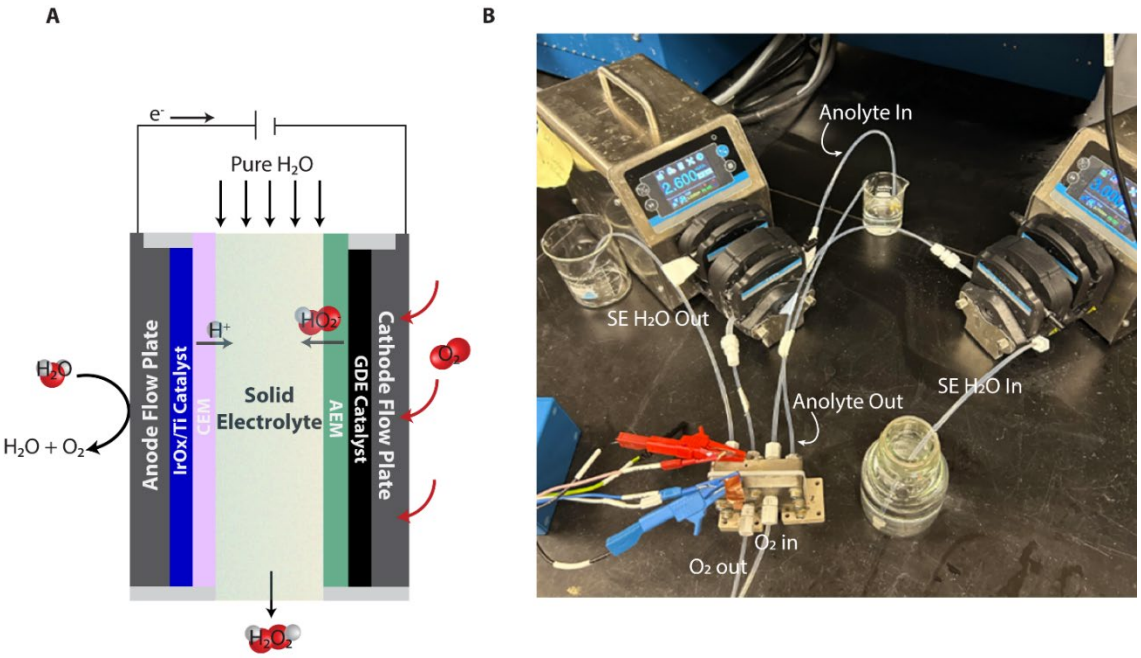

Figure S2. A) Schematic and B) set-up demonstration of H_2O_2 electrosynthesis in a two-electrode dual membrane electrode assembly (MEA) solid electrolyte flow cell. Note schematic not drawn to scale.

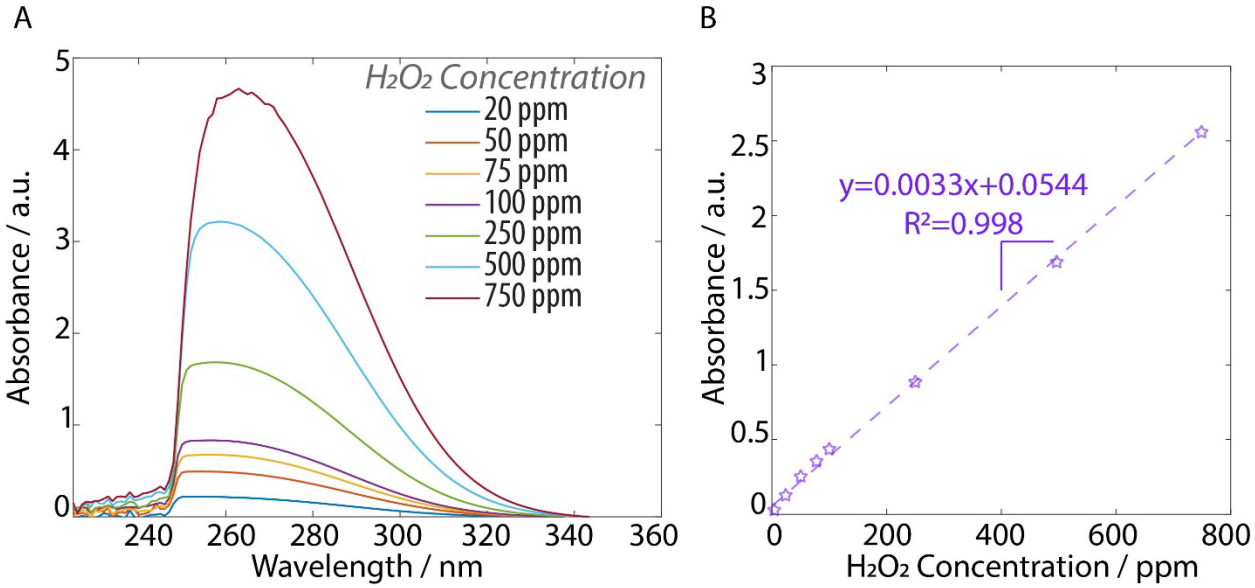

Figure S3. H_2O_2 quantification. A) UV-vis spectra of Co/CO_3 assay with various concentrations of H_2O_2 (ppm) and B) its corresponding calibration curve.

The produced H_2O_2 was quantified using a cobalt-carbonate (Co/CO_3) assay coupled with UV-vis spectrophotometry.[1] The Co/CO_3 assay contains a mixture of $KHCO_3$ and cobalt sulfate heptahydrate ($CoSO_4 \cdot 7H_2O$) both of which dissociate in water and exhibit a light pink color solution. H_2O_2 oxidizes Co^{2+} in the presence of bicarbonate likely forming a 'carbonatocobaltate' complex ($Co(CO_3)_3^{3-}$) which strongly absorbs at 290 nm and weakly in the visible region (440 and 635 nm), exhibiting a dark green color. The 290 nm feature was used for quantification unless otherwise specified. The absorbance of the $Co(CO_3)_3^{3-}$ complex is measured which is linearly proportional to the concentration of H_2O_2 present. The Co/CO_3 assay was prepared by first mixing 1.35 mL of 2 M $KHCO_3$ and 35.8 µl of 2 mM $CoSO_4 \cdot 7H_2O$ in a cuvette. Next, 35.8 µl of our H_2O_2 sample (known or unknown concentration) was added to the cuvette and mixed. Immediately afterward, 1.425 mL of 2 M $KHCO_3$ was added to the cuvette and mixed. The absorbance of these samples was measured in the wavelength range 200-800 nm with 1 nm resolution and scanning rate of 2 nm/s (Agilent Cary 6000i). The UV-vis spectra were background-subtracted using a baseline measurement of the same analyte solutions with 35.8 µl of H_2O added instead of H_2O_2 containing samples. A typical calibration curve was plotted by linear fitting the absorbance values at wavelength of 290 nm for various known concentrations of H_2O_2 from 20 ppm to 750 ppm.

Section S2. Material Characterization

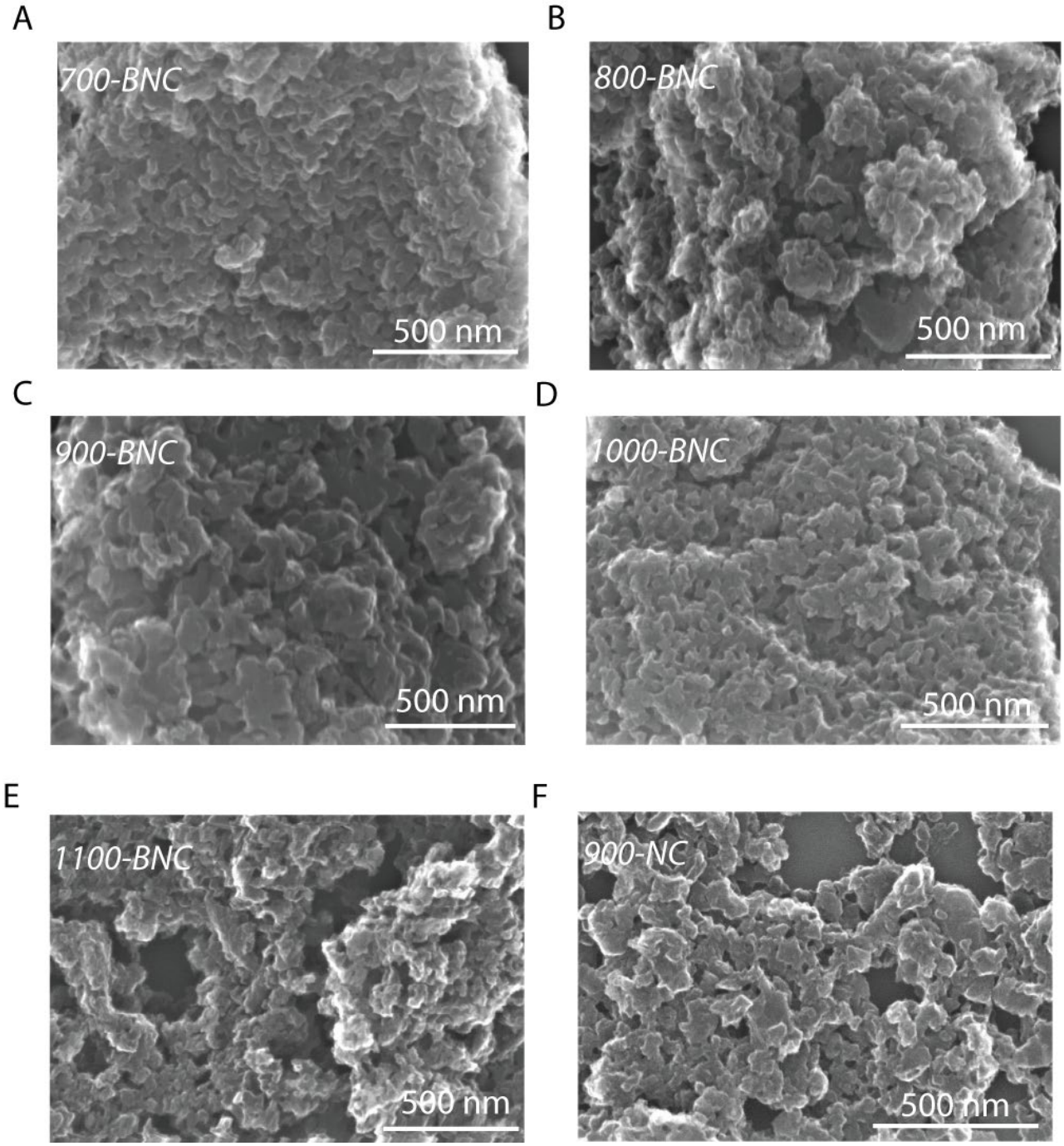

Figure S4. Scanning electron microscopy (SEM) reveals morphological evolution of the BNC catalysts pyrolyzed at A) 700°C, B) 800°C, C) 900°C, D) 1000°C, and E) 1100°C. F) Nitrogen doped carbon pyrolyzed at 900°C (900-NC).

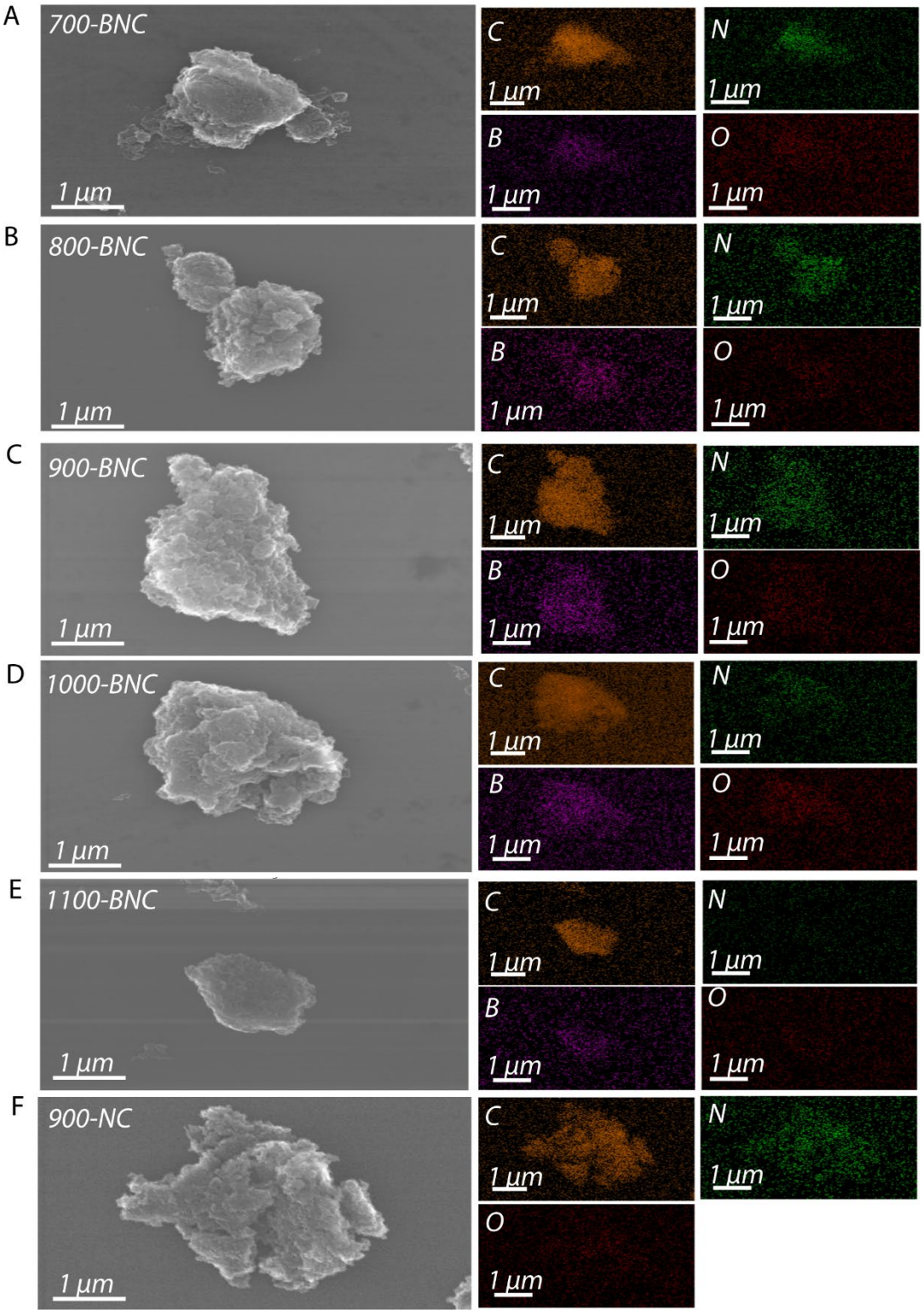

Figure S5. Energy dispersive spectroscopy (EDS) elemental mapping of the BNC catalysts pyrolyzed at A) 700°C, B) 800°C, C) 900°C, D) 1000°C, and E) 1100°C. F) Nitrogen doped carbon pyrolyzed at 900°C (900-NC).

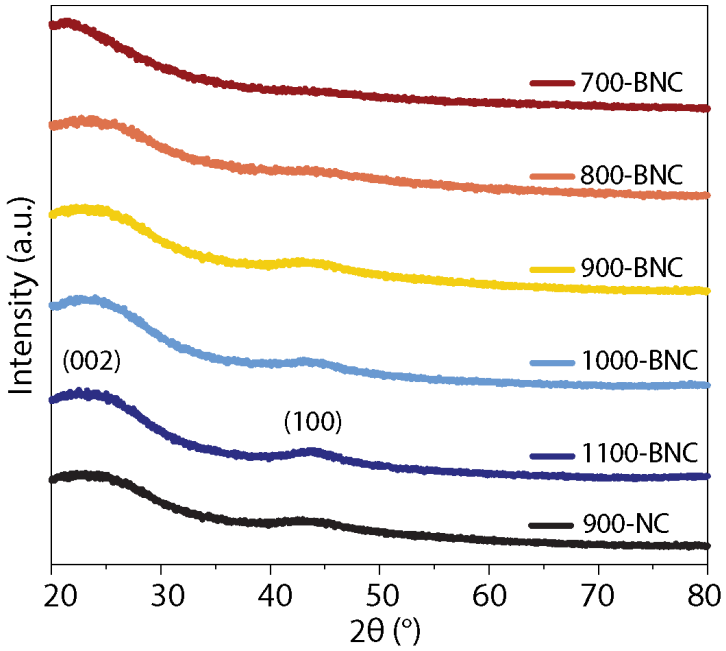

Figure S6. Powder X-ray diffraction (XRD) patterns of the as-prepared catalysts.

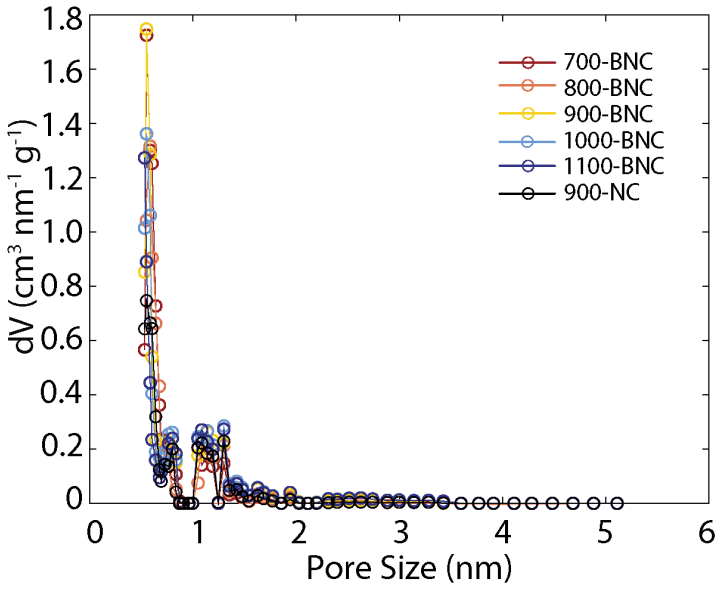

Figure S7. Pore size distributions of the as-prepared catalysts derived non-local density functional theory analysis of N_2 adsorption-desorption isotherms.

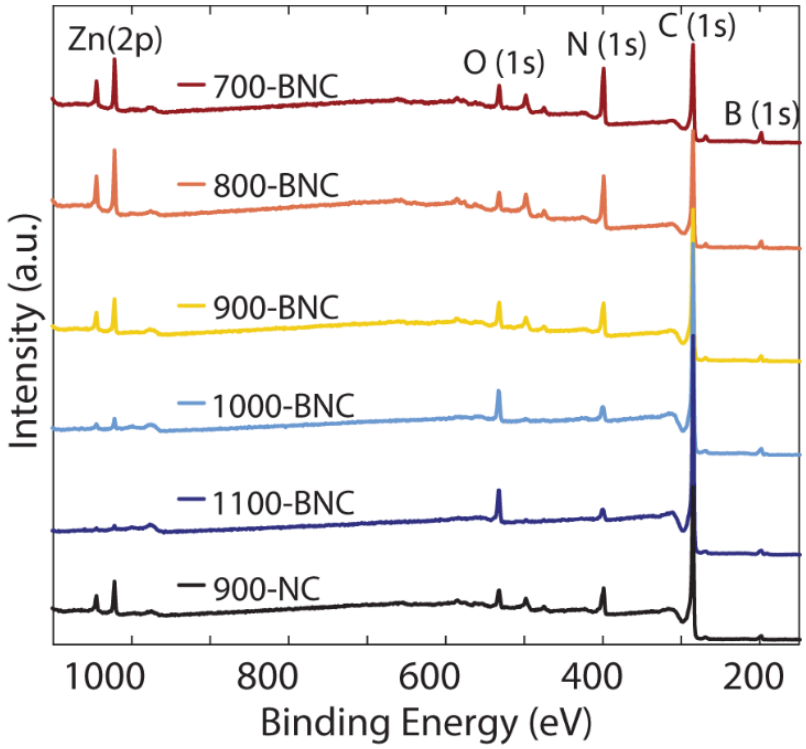

Figure S8. X-ray photoelectron spectroscopy (XPS) survey spectra of the BNC and NC catalysts.

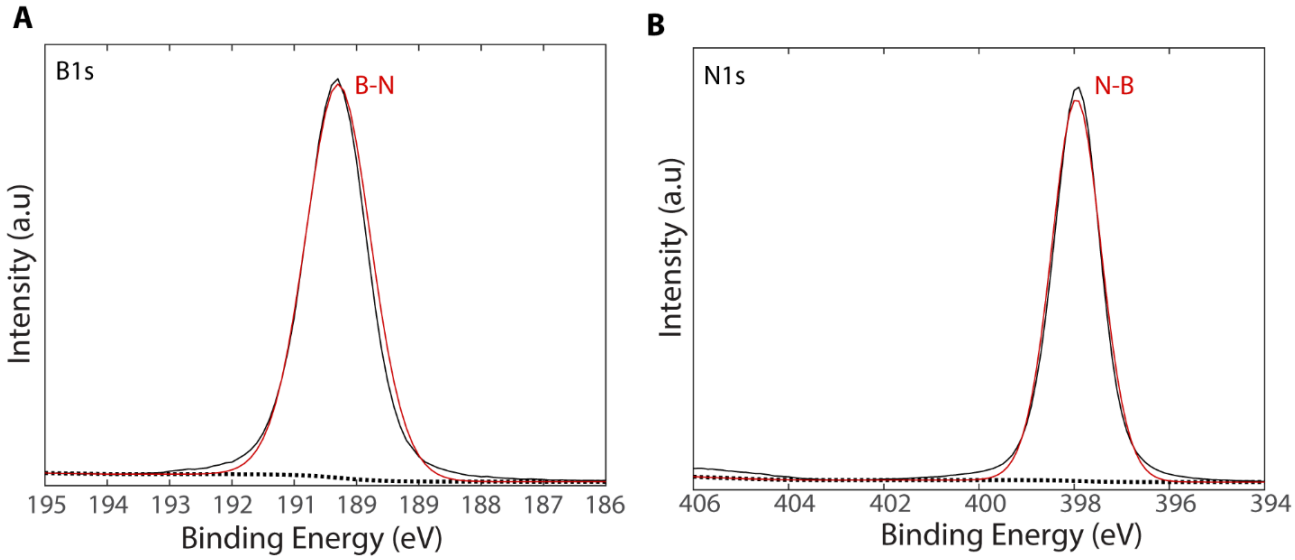

Figure S9. Fitting for A) B1s and B) N1s XPS spectra for boron nitride (*h*-BN) reference material derived from XPS measurements.

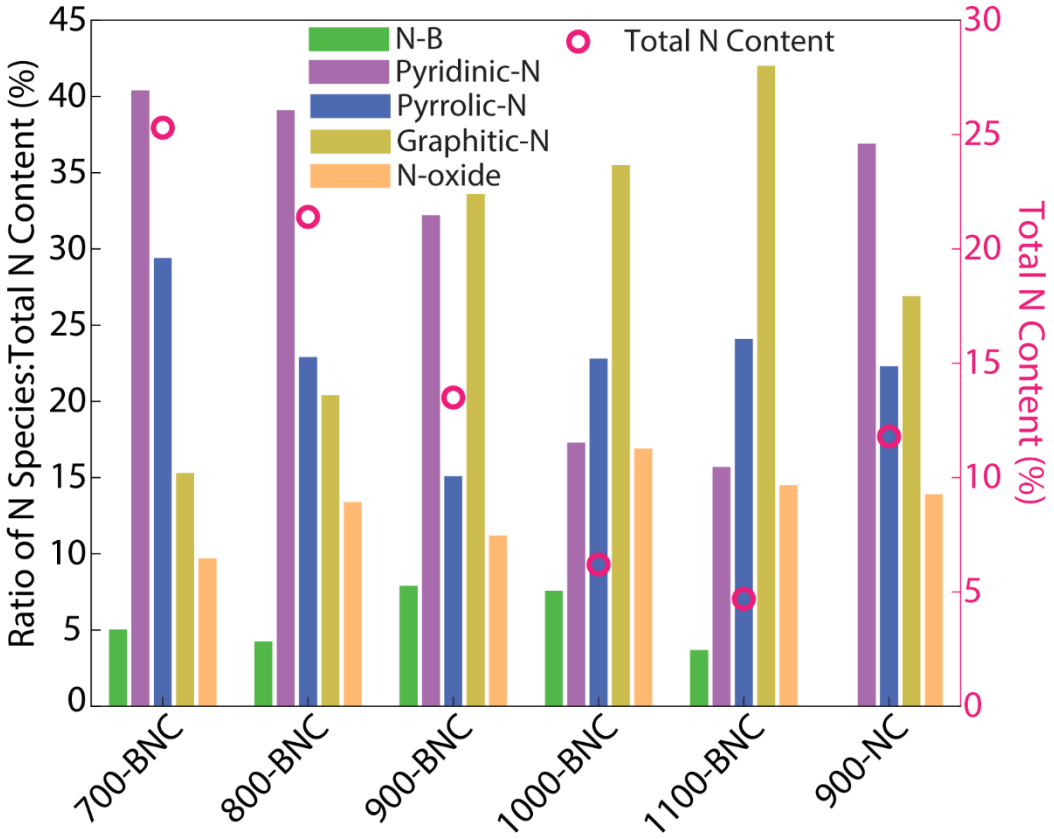

Figure S10. Ratio of nitrogen species to total nitrogen content in as-prepared BNC samples derived from XPS measurements. 900-NC included for comparison.

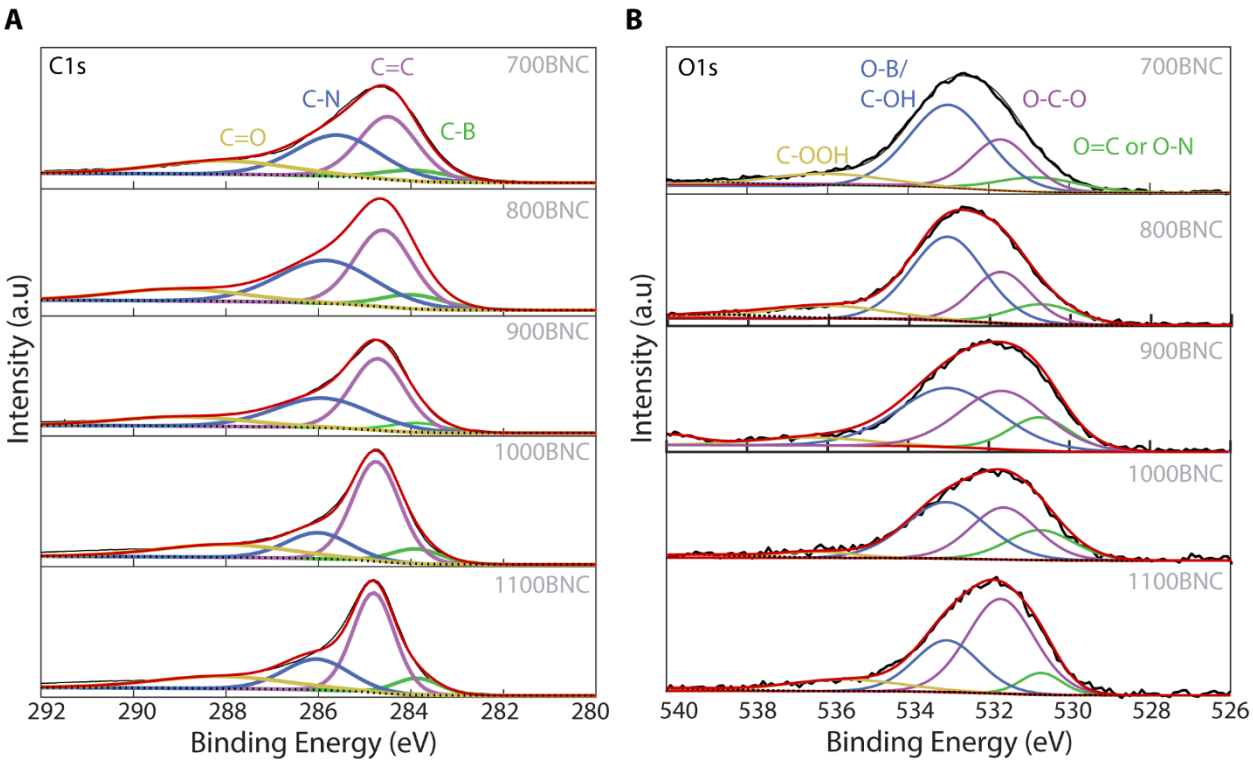

Figure S11. Deconvoluted A) C 1s and B) O 1s XPS spectra of BNC catalysts.

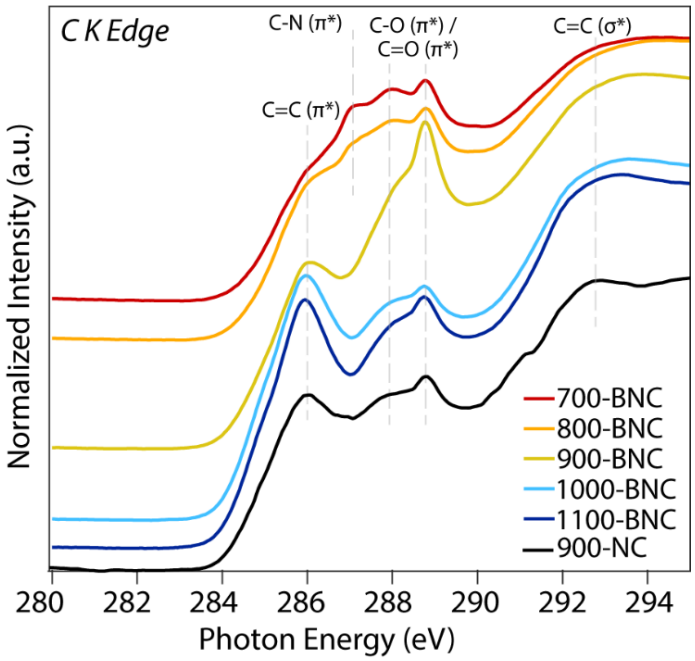

Figure S12. Carbon K-edge X-ray absorption spectroscopy (XAS) spectra for the different as-prepared catalysts.

Section S2. Rotating Ring-Disk Electrode Measurements

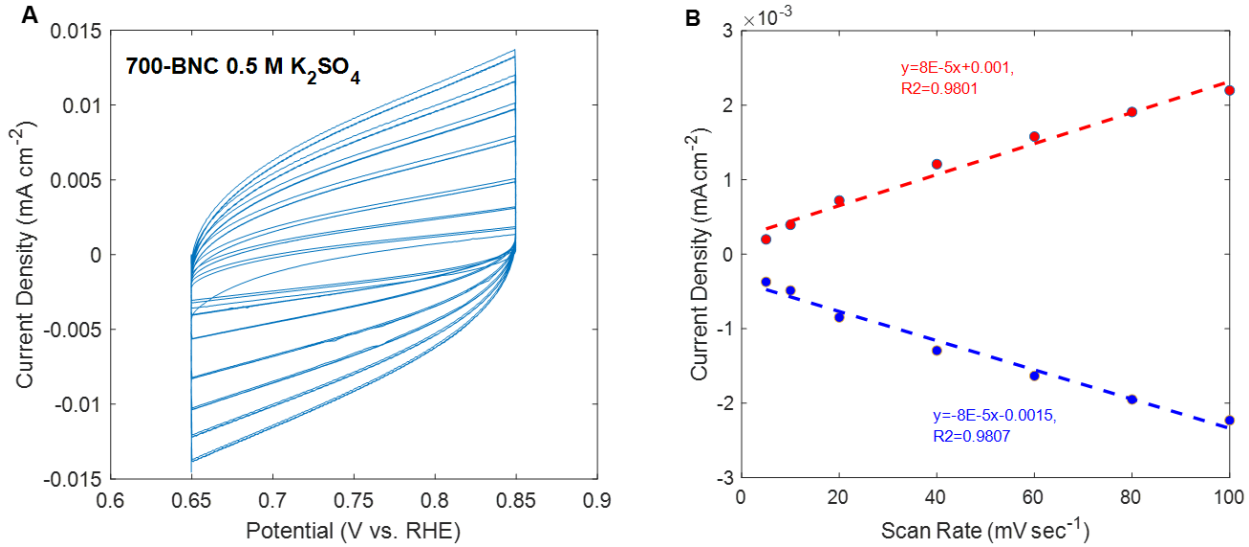

Figure S13. A) Cyclic voltammogram (CV) curves of 700-BNC in the double layer region at scan rates 5, 10, 20, 40, 60, 80, and 100 mV s^{-1} in 0.5 M K_2SO_4 aqueous electrolyte; B) Current density (taken at 0.75 V vs. RHE) as a function of scan rate derived from CV curves.

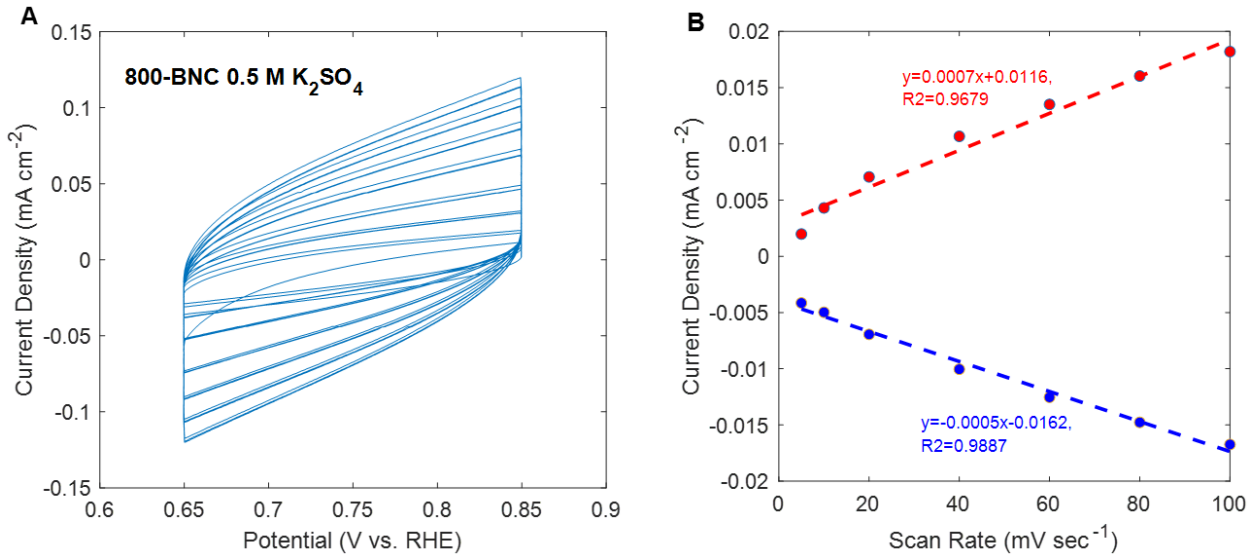

Figure S14. A) Cyclic voltammogram (CV) curves of 800-BNC in the double layer region at scan rates 5, 10, 20, 40, 60, 80, and 100 mV s^{-1} in 0.5 M K_2SO_4 aqueous electrolyte; B) Current density (taken at 0.75 V vs. RHE) as a function of scan rate derived from CV curves.

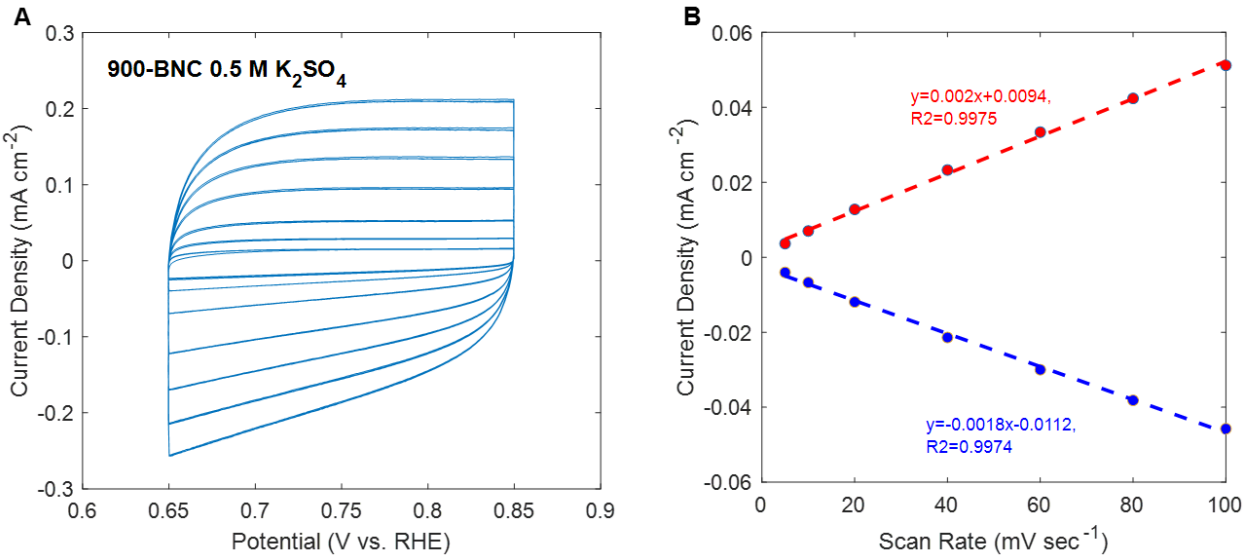

Figure S15. A) Cyclic voltammogram (CV) curves of 900-BNC in the double layer region at scan rates 5, 10, 20, 40, 60, 80, and 100 mV s^{-1} in 0.5 M K_2SO_4 aqueous electrolyte; B) Current density (taken at 0.75 V vs. RHE) as a function of scan rate derived from CV curves.

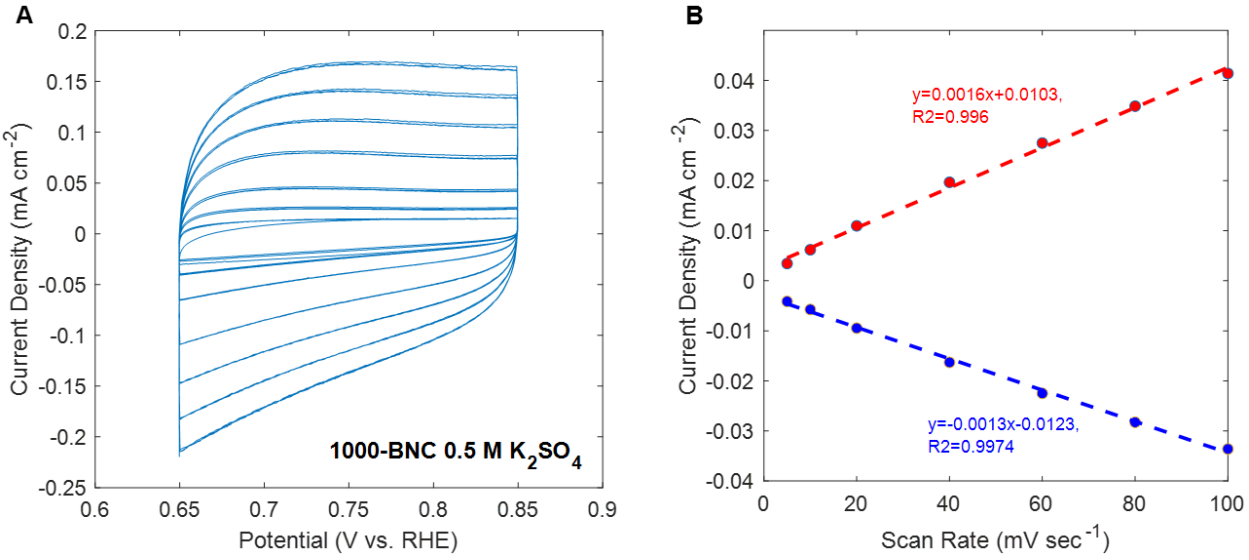

Figure S16. A) Cyclic voltammogram (CV) curves of 1000-BNC in the double layer region at scan rates 5, 10, 20, 40, 60, 80, and 100 mV s^{-1} in 0.5 M K_2SO_4 aqueous electrolyte; B) Current density (taken at 0.75 V vs. RHE) as a function of scan rate derived from CV curves.

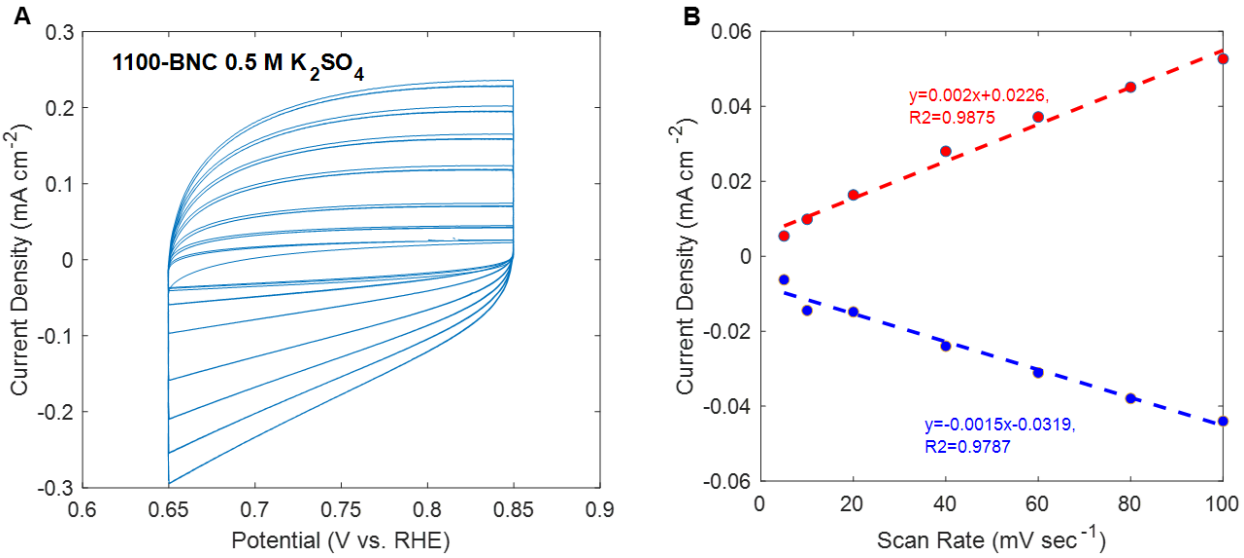

Figure S17. A) Cyclic voltammogram (CV) curves of 1100-BNC in the double layer region at scan rates 5, 10, 20, 40, 60, 80, and 100 mV s^{-1} in 0.5 M K_2SO_4 aqueous electrolyte; B) Current density (taken at 0.75 V vs. RHE) as a function of scan rate derived from CV curves.

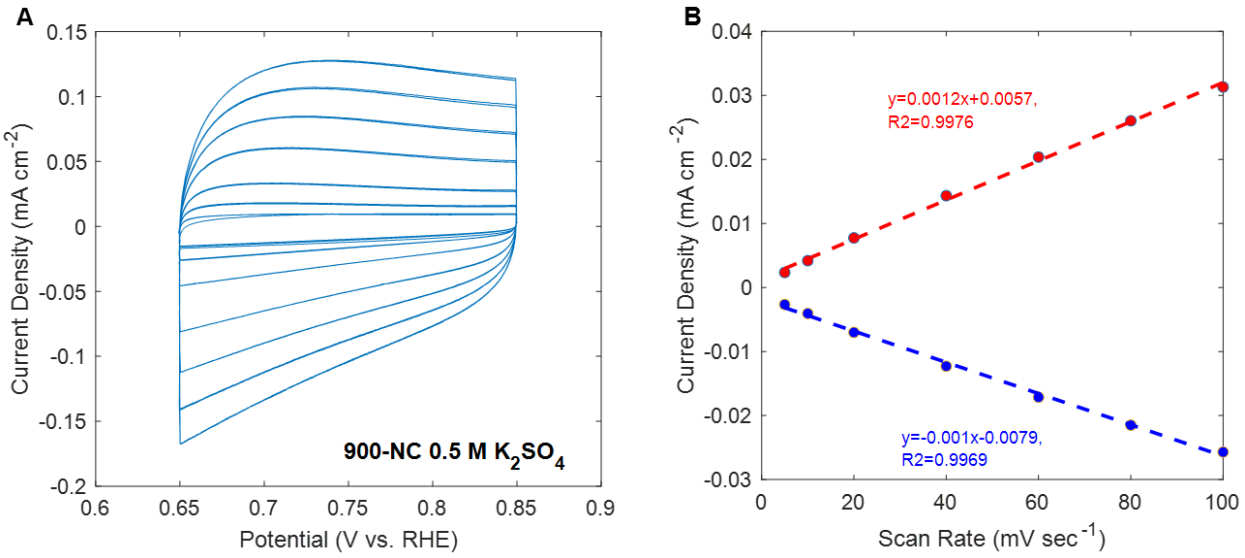

Figure S18. A) Cyclic voltammogram (CV) curves of 900-NC in the double layer region at scan rates 5, 10, 20, 40, 60, 80, and 100 mV s^{-1} in 0.5 M K_2SO_4 aqueous electrolyte; B) Current density (taken at 0.75 V vs. RHE) as a function of scan rate derived from CV curves.

Electrochemically active surface area (ECSA) was estimated by measuring the electrochemical double-layer capacitance (C_{dl}, Fig. S13-S18) via performing multiple CV curves over a 0.20 V potential range near the open circuit voltage (OCV) where no Faradaic reaction occurs with various scan rates between 5 to 100 mV s^{-1}. The double layer capacitance is calculated as

follows: $C_{dl} = J/\frac{dV}{dt}$ where J is the current density at the center of the potential range, C_{dl} is the capacitance, and dV/dt represents the CV scan rate.

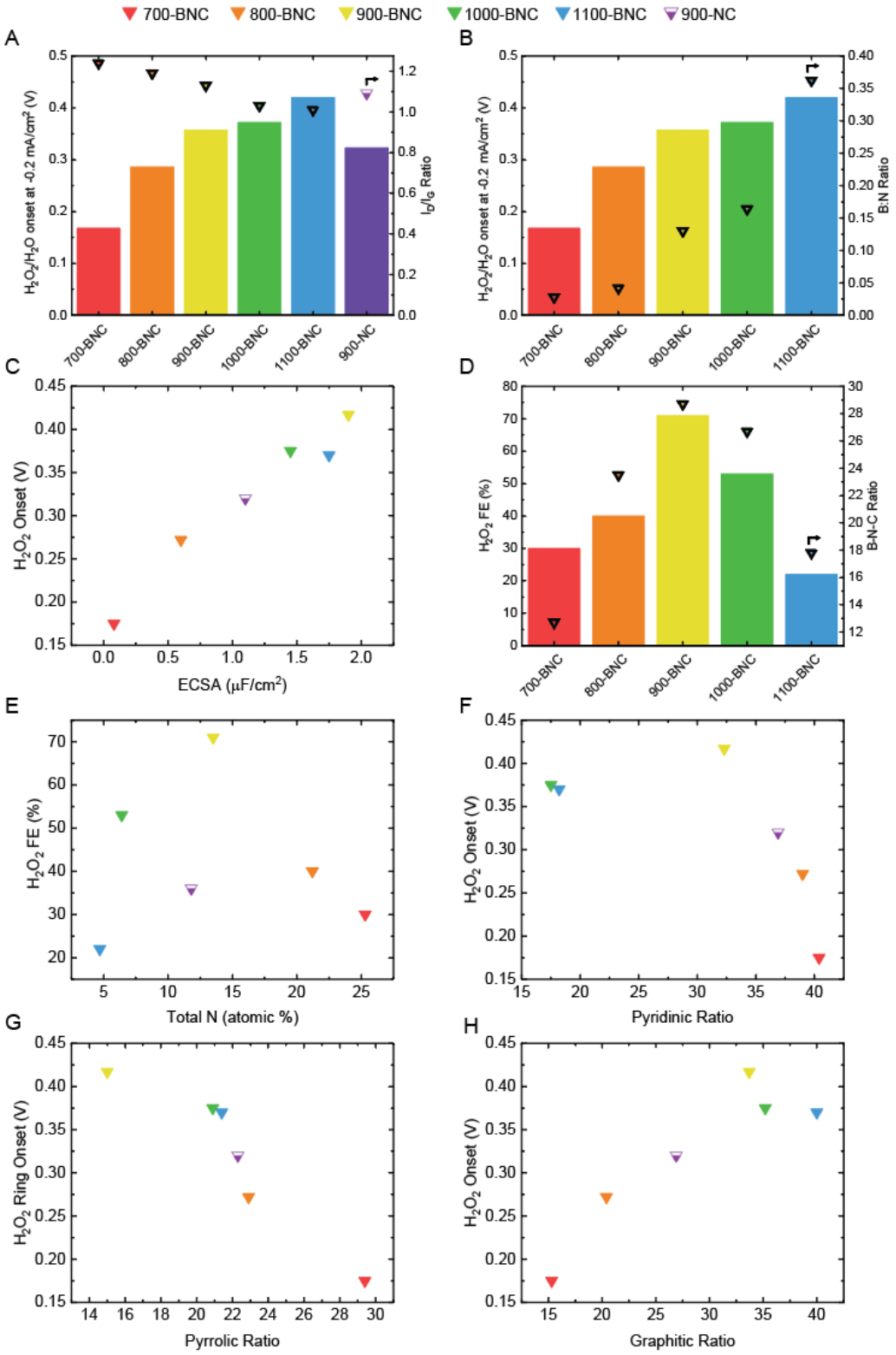

Figure S19. A) H_2O_2/H_2O onset potential at -0.2 mA/cm^2 disk vs. I_D/I_G ratio measured by Raman. B) H_2O_2/H_2O onset potential at -0.2 mA/cm^2 disk vs. B:N ratio measured by XPS. C) H_2O_2 ring overpotential vs. ECSA measured by double-layer capacitance of catalysts. D) H_2O_2

ring overpotential vs. pyrrolic ratio measured by XPS. E) Maximum H_2O_2 FE vs. graphitic ratio measured by XPS. F) Maximum H_2O_2 FE vs. pyridinic ratio measured by XPS. G) Maximum H_2O_2 FE vs. B-N-C ratio measured by XPS. H) Maximum H_2O_2 FE vs. total N content measured by XPS. Ratios represent the relative content of specified species compared to the total content. Values are displayed in Table S1, S4, and S5.

Figure S19 displays the key performance metrics as a function of the catalyst material properties. Figure S19A-B demonstrates the improvement in H_2O_2/H_2O onset potential (overall ORR onset) trends with a higher degree of graphitization (I_D/I_G ratio) and an increase in the B:N ratio. Figure S19C displays a linear relationship between H_2O_2 (ring) onset potential and ECSA. Figure S19D further shows how a higher content of local B-N-C dopant configurations leads to a more favorable selectivity toward H_2O_2. Figure S19E-H explores the relationship between N content and configurations with respect to H_2O_2 performance. Figure S19E shows how moderate N doping is more favorable for $2e^-$ ORR to H_2O_2. Figure S19F-G shows how pyrrolic and pyridinic moieties impede H_2O_2 formation, while Figure S19H demonstrates how graphitic-N improves H_2O_2 performance.

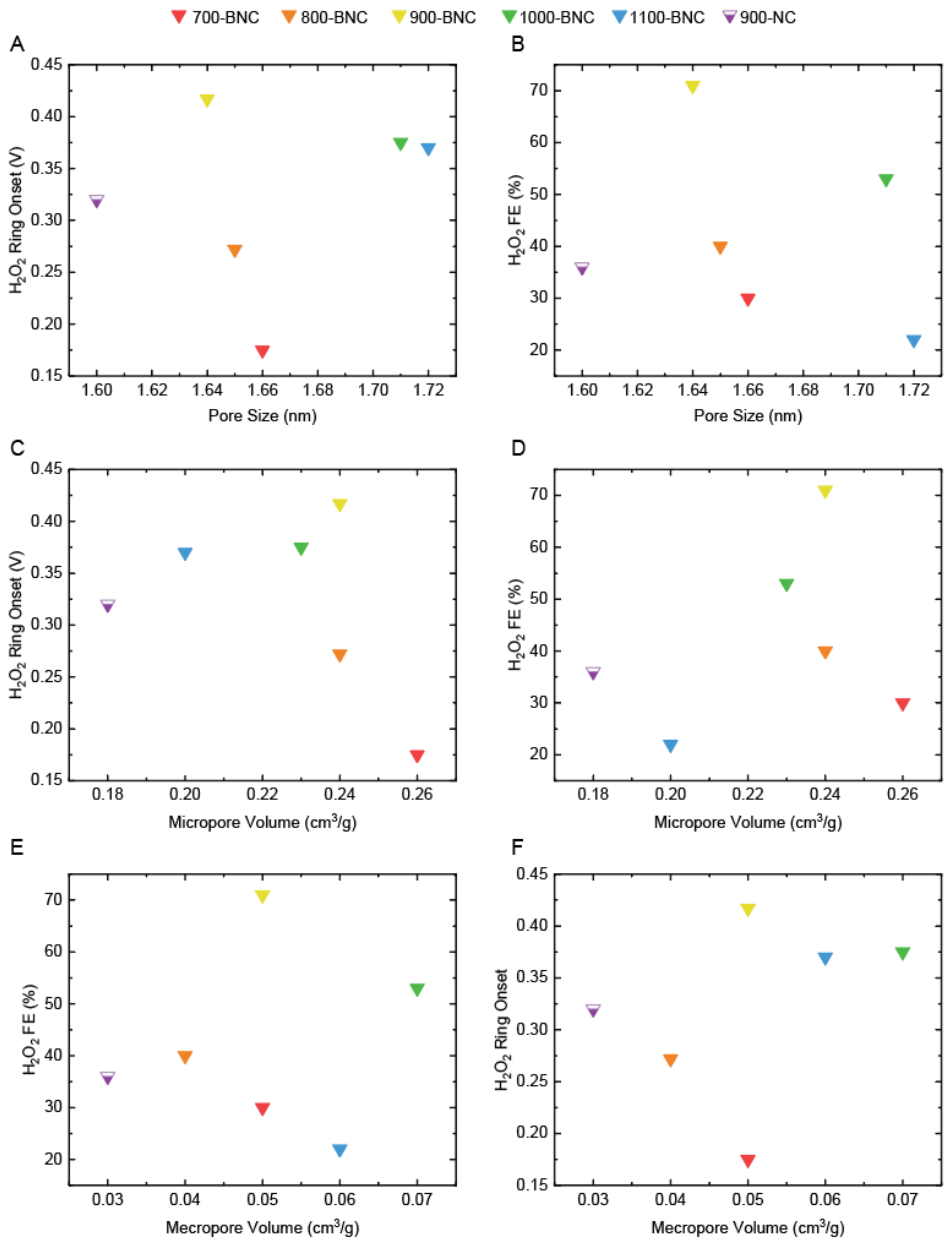

Figure S20. A) H_2O_2 ring overpotential vs. pore size measured by N_2 adsorption. B) Maximum H_2O_2 FE vs. pore size. C) H_2O_2 ring overpotential vs. micropore volume measured by N_2 adsorption. D) Maximum H_2O_2 FE vs. micropore volume. E) H_2O_2 ring overpotential vs. mesopore volume measured by N_2 adsorption. F) Maximum H_2O_2 FE vs. mesopore volume. Values are displayed in Table S2.

Figure S20 displays the effects of pore size, micropore volume, and mesopore volume on the performance of H_2O_2 electrosynthesis (activity onset and FE). No significant contribution to changes in performance is observed with varying pore structures.

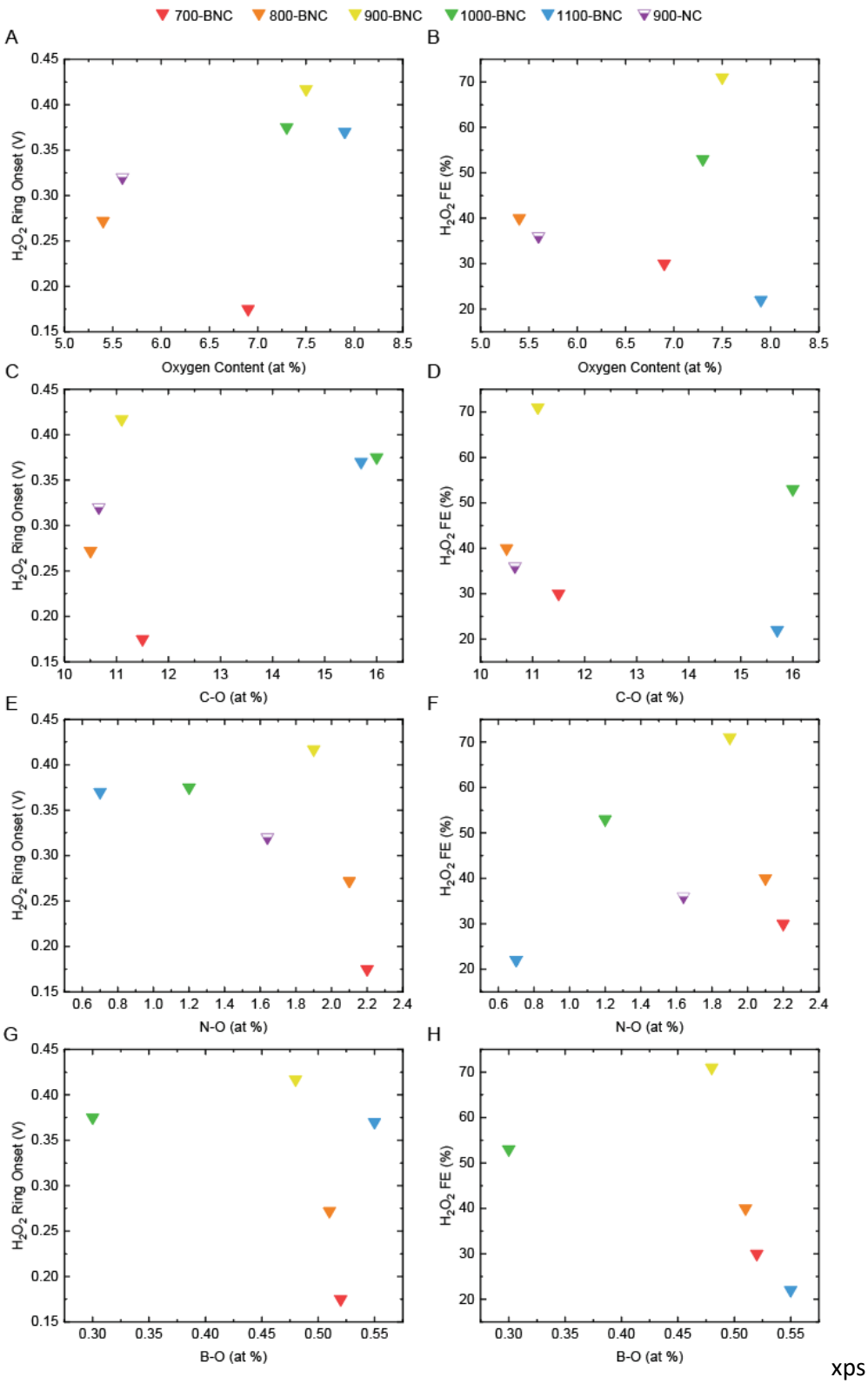

Figure S21. A) H_2O_2 ring overpotential vs. O content measured by XPS. B) Maximum H_2O_2 FE vs. O content. C) H_2O_2 ring overpotential vs. C-O bond ratio measured by XPS. D) Maximum H_2O_2 FE vs. C-O bond ratio. E) H_2O_2 ring overpotential vs. N-O bond ratio measured by XPS. F)

Maximum H_2O_2 FE vs. N-O bond ratio. G) H_2O_2 ring overpotential vs. B-O bond ratio measured by XPS. H) Maximum H_2O_2 FE vs. B-O bond ratio. Values are displayed in Table S3-6.

Figure S21 shows the effect of O in BNC and NC catalysts on H_2O_2 electrosynthesis performance. The total O content and amount of C-O bonds do not affect the performance. The H_2O_2 FE shows a maximum at 1.9 at % N-O bonds (out of all N bonds) and 0.48 at % B-O bonds (out of all B bonds).

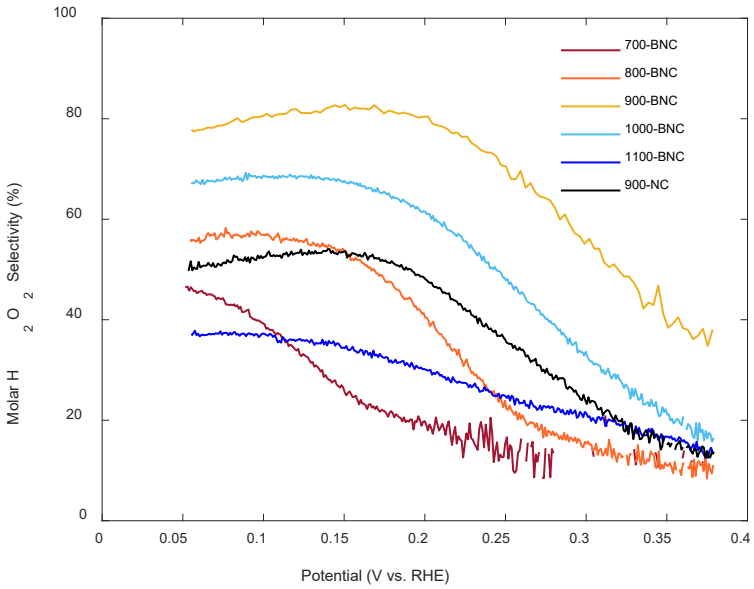

Figure S22. Calculated molar H_2O_2 selectivity as a function of applied potential for the different BNC catalysts in 0.5 M K_2SO_4. 900-NC is included for comparison.

Section S3. Electrochemical Flow Cell Measurements

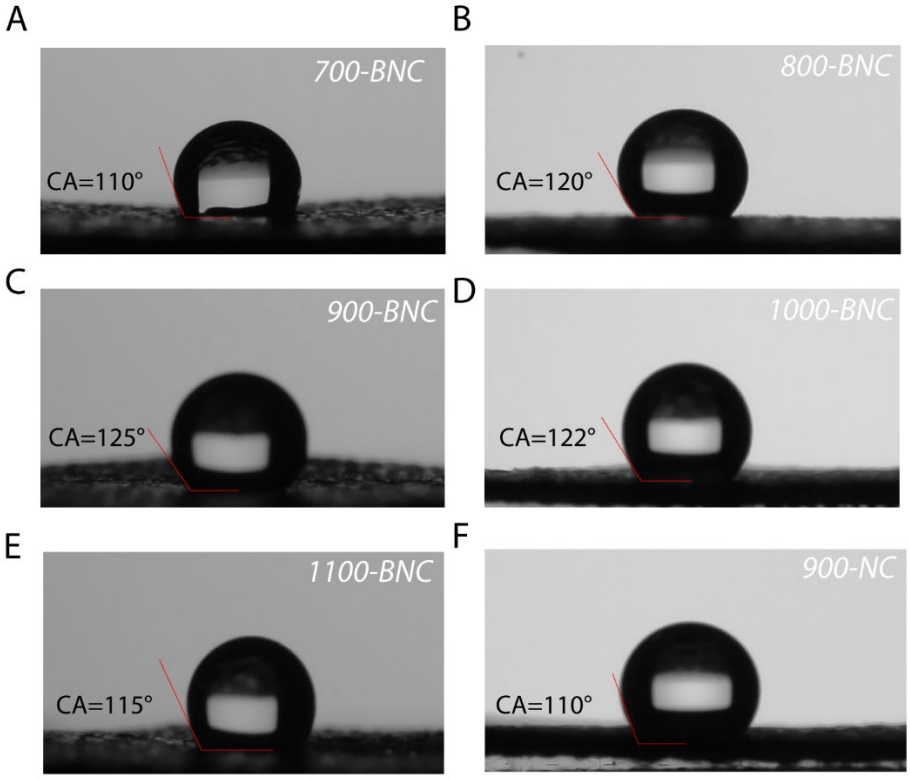

Figure S23. Contact angle measurements for the as-prepared catalysts spray coated on a carbon cloth electrode. A) 700-BNC, B) 800-BNC, C) 900-BNC, D) 1000-BNC, E) 1100-BNC, and F) 900-NC.

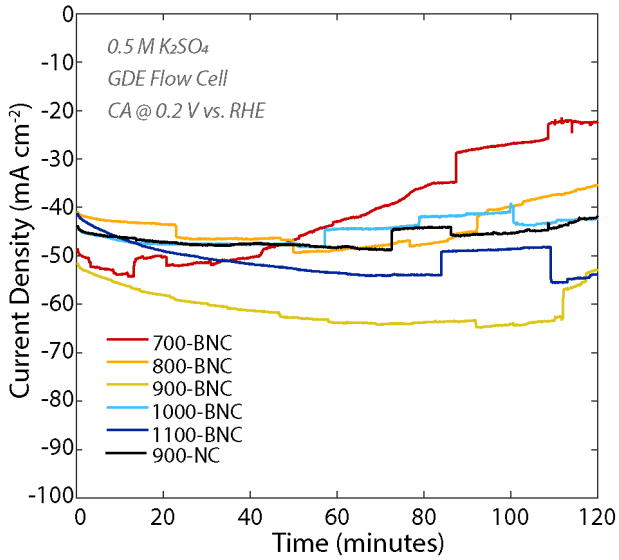

Figure S24. Chronoamperometry (CA) held at 0.20 V vs. RHE for 2 hours for different BNC catalysts in 0.5 M K_2SO_4 in three-electrode gas diffusion electrode (GDE) flow cell. 900-NC included for comparison.

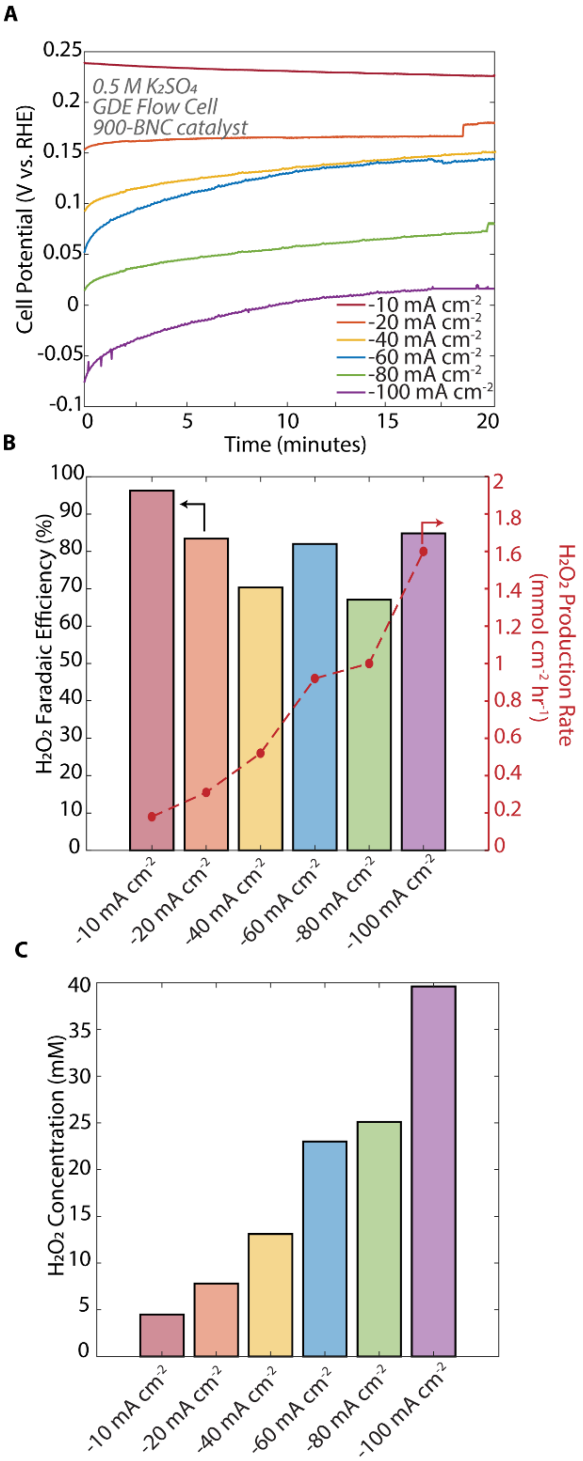

Figure S25. Chronopotentiometry (CP) measurements held for 15 minutes at different applied current densities (-10, -20, -40, -60, -80, and -100 mA cm^{-2}) for 900-BNC catalyst in three-electrode GDE flow cell. A) Cell potential vs. time. B) H_2O_2 Faradaic efficiency (right axis) and H_2O_2 production rate (left axis). C) Final H_2O_2 concentration measured after 15 minutes under various applied current densities.

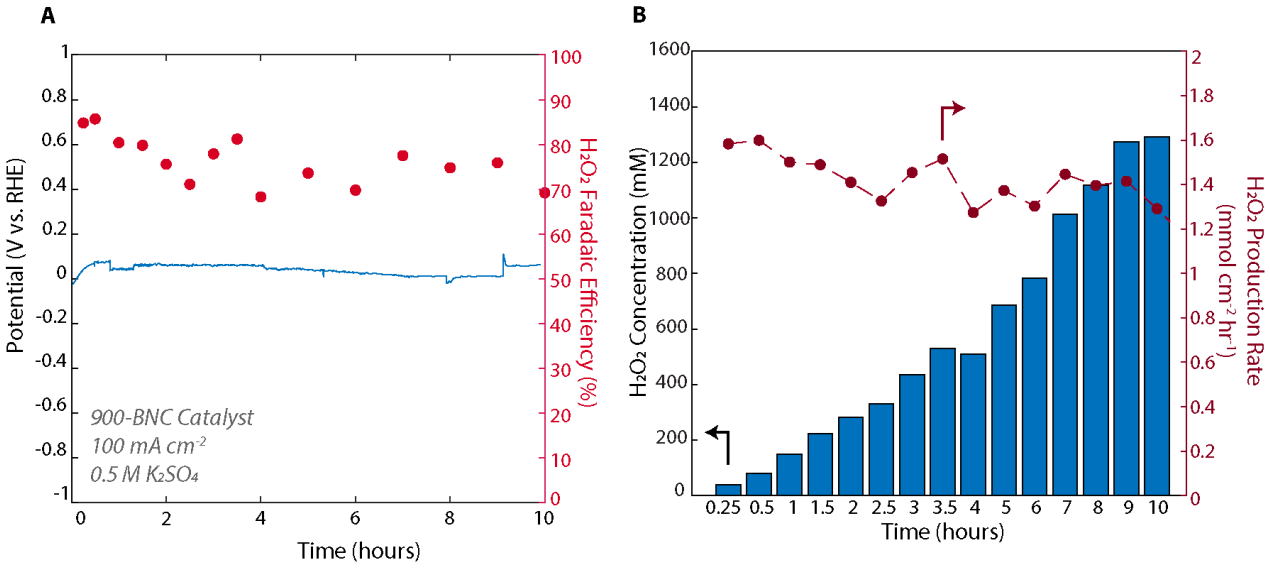

Figure S26. Stability test of 900-BNC in a three-electrode GDE flow cell at 100 mA cm^{-2} in 0.5 M K_2SO_4 electrolyte. A) Corresponding potential response (left axis) and H_2O_2 Faradaic efficiency (right axis). C) H_2O_2 concentration measured over 10 hours (left axis) and calculated H_2O_2 production rate (right axis). H_2O_2 was collected in the recycled catholyte stream.

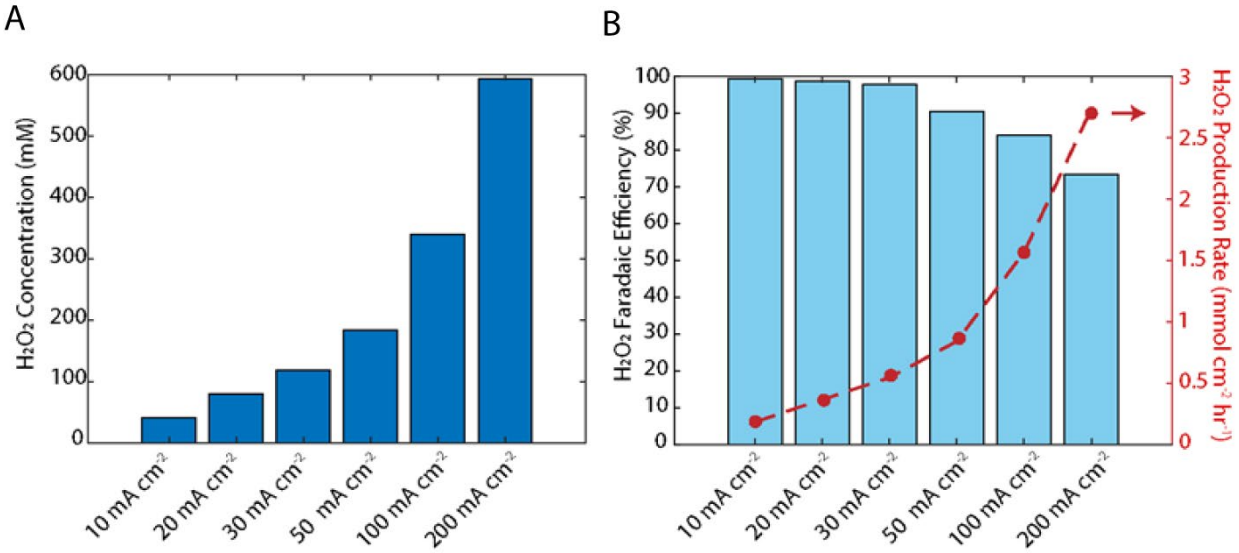

Figure S27. H_2O_2 production performance for 900-BNC in a two-electrode MEA solid electrolyte flow cell as a function of applied current density. A) Measured H_2O_2 concentration and corresponding B) Faradaic efficiency (right axis) and production rate (left axis) measured after 30 minutes. H_2O_2 was collected as a single pass rinse through solid electrolyte chamber.

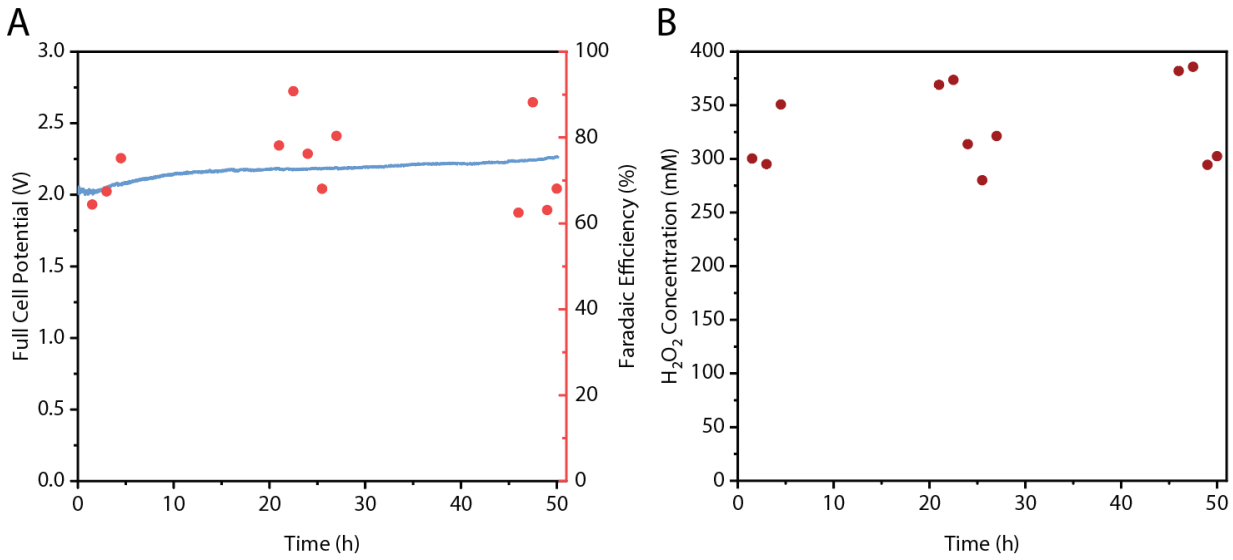

Figure S28. H_2O_2 production stability test for 900-BNC in a two-electrode MEA solid electrolyte flow cell as a function of applied current density. A) Full cell potential and corresponding Faradaic efficiency (right axis) and B) H_2O_2 concentration over chronopotentiometry hold at 50 mA cm^{-2}. H_2O_2 was collected as a single pass rinse through solid electrolyte chamber

Section S4. Supplementary Tables

Table S1. Raman I_D/I_G intensity band ratios.

Sample	D Band Intensity (1350 cm^{-1})	G Band Intensity (1580 cm^{-1})	I_D/I_G Ratio
700-BNC	10400	8400	1.24
800-BNC	11300	9500	1.19
900-BNC	5200	4610	1.13
1000-BNC	5730	5546	1.03
1100-BNC	1420	1400	1.01
900-NC	1655	1521	1.09

Table S2. N_2 adsorption-desorption isotherms.

Sample	Specific Surface Area (m^2/g)[a]	Total Pore Volume (cm^3/g)[a]	Micropore Volume (cm^3/g)[b]	Mesopore Volume (cm^3/g)[c]	Average Pore Width (nm)[d]
700-BNC	760	0.31	0.26	0.05	1.66
800-BNC	680	0.28	0.24	0.04	1.65
900-BNC	715	0.29	0.24	0.05	1.64
1000-BNC	700	0.30	0.23	0.07	1.71
1100-BNC	620	0.26	0.20	0.06	1.72
900-NC	530	0.21	0.18	0.03	1.60

a – specific surface area and total pore volume is a calculated with BET theory
b – micropore volume is calculated with t-plot value
c – mesopore volume is the difference of single pore volume and t-plot micropore volume
d – pore size is calculated with a non-local density functional theory model assuming slit carbon pores

Table S3. Elemental analysis of the catalyst materials obtained by different temperature treatments derived from XPS measurements.

Sample	C at%	N at%	O at%	Zn at%	B at%	B:N ratio
700-BNC	64.6	25.2	6.9	2.6	0.71	0.028
800-BNC	68.6	21.7	5.4	3.2	0.98	0.045
900-BNC	75.4	13.8	7.5	1.6	1.78	0.130
1000-BNC	85.0	6.3	7.3	0.4	1.01	0.161
1100-BNC	85.6	4.7	7.9	0.2	1.63	0.350
900-NC	80.9	11.7	5.6	1.8	-	-

Table S4. Elemental analysis of the different boron species in the catalyst materials derived from XPS measurements. The ratio represents the percentage of a specific B functional group in the total B content. The atom percent (at%) reflects the amount of a certain B functional group in the entire material.

Sample	Total B at%	B-N-C ratio/**at%** (190 eV)	B-N ratio/**at%** (191 eV)	B-O ratio/**at%** (192 eV)	*Total B-N + B-N-C ratio*
700-BNC	0.71	12.7 / **0.09**	14.1 / **0.10**	73.2 / **0.52**	*26.8*
800-BNC	0.98	23.5 / **0.23**	24.5 / **0.24**	52.0 / **0.51**	*48.0*
900-BNC	1.78	28.7 / **0.51**	44.4 / **0.79**	27.0 / **0.48**	*73.0*
1000-BNC	1.01	26.7 / **0.27**	43.6 / **0.44**	29.7 / **0.30**	*70.3*
1100-BNC	1.63	17.8 / **0.29**	48.5 / **0.79**	33.7 / **0.55**	*66.3*

Table S5. Elemental analysis of the different nitrogen species in the catalyst materials derived from XPS measurements. The ratio represents the percentage of a specific N functional group in the total N content. The atom percent (at%) reflects the amount of a certain N functional group in the entire material.

Sample	Total N at%	N-B ratio/**at%** (397.7 eV)	Pyridinic ratio/**at%** (398.5 eV)	Pyrrolic ratio/**at%** (399.5 eV)	Graphitic ratio/**at%** (400.7 eV)	N-oxide ratio/**at%** (403.5 eV)	*Total N-C ratio*
700-BNC	25.2	4.0 / **1.0**	46.1 / **11.7**	28.2 / 7.1	13.2 / 3.4	8.5 / **2.2**	*87.5*
800-BNC	21.7	4.8 / **1.1**	45.5 / **9.9**	27.0 / **5.9**	12.9 / **2.8**	9.8 / **2.1**	*85.3*
900-BNC	13.8	7.5 / **1.0**	39.2 / **5.4**	18.3 / **2.5**	21.2 / **2.9**	13.8 / **1.9**	*78.7*
1000-BNC	6.3	6.1 / **0.38**	17.7 / **1.1**	21.2 / **1.3**	35.8 / **2.24**	19.2 / **1.2**	*74.8*
1100-BNC	4.7	5.6 / **0.26**	18.1 / **0.84**	19.8 / **0.92**	41.4 / **1.9**	15.1 / **0.7**	*79.3*
900-NC	11.7	-	36.9 / **4.34**	22.3 / **2.63**	26.9 / **3.17**	13.9 / **1.64**	*86.1*

Table S6. Elemental analysis of the different carbon species in the catalyst materials derived from XPS measurements. The ratio represents the percentage of a specific C functional group in the total C content. The atom percent (at%) reflects the amount of a certain C functional group in the entire material.

Sample	Total C at%	C-B ratio/**at%** (283.9 eV)	C=C ratio/**at%** (284.5 eV)	C-N ratio/**at%** (286 eV)	C-O ratio/**at%** (288.3 eV)	*Total C-B + C-N ratio*
700-BNC	64.6	7.8 / **5.0**	37.7 / **24.3**	36.8 / **23.7**	17.8 / **11.5**	*44.5*
800-BNC	68.6	7.8 / **5.4**	39.7 / **27.5**	37.4 / **25.9**	15.1 / **10.5**	*45.1*
900-BNC	75.4	6.1 / **4.6**	46.0 / **34.9**	33.3 / **25.3**	14.6 / **11.1**	*39.4*
1000-BNC	85.0	8.7 / **7.4**	53.6 / **45.5**	18.9 / **16.0**	18.9 / **16.0**	*27.6*
1100-BNC	85.6	9.1 / **7.8**	48.9 / **41.7**	23.6 / **20.1**	18.4 / **15.7**	*32.7*

Lower concentration of C-B suggests higher concentration of B-N-C moieties are present.

Table S7. Calculated partial H_2O_2 kinetic current density values at 0.20 V vs. RHE.

Catalyst	**H_2O_2 Kinetic Current Density ($J_{kin, H2O2}$)**
700-BNC	0.012
800-BNC	0.16
900-BNC	0.82
1000-BNC	0.58
1100-BNC	0.29
900-NC	0.22

Table S8. Catholyte composition of boron measured via ICP-MS after electrochemical testing for 2 hours at 0.20 V vs. RHE.

Sample	Boron (ppm)
700-BNC	0.016
800-BNC	0.011
900-BNC	0.015
1000-BNC	0.012
1100-BNC	0.009
0.5 M K_2SO_4	0.007

Based on an initial catalyst loading of 0.5 mg/cm^2 for the 900-BNC electrode that contains 9 μg of total B, ICP-MS results indicate that only 0.08 μg B dissolved in the catholyte after 2 hours of ORR testing, corresponding to < 1 % dissolution. This suggests that the boron content of the 900-BNC catalyst remains highly stable under the explored reaction conditions.

Table S9. Comparison of H_2O_2 performance of different carbon-based catalysts using RRDE.

Material	*pH*	*Onset Potential (V_{RHE})*	*H_2O_2 Selectivity (%)*	*Reference*
Boron nitride islands	0.1 M KOH	0.8	78	[8]
Mesoporous nitrogen carbon (MNC-600)	0.1 M $KHCO_3$	0.7	85	[9]
Hierarchically porous carbon	7	0.16	70.8	[10]
Activated carbon/carbon fiber	7	0.31	26.5	[11]
NCMK3IL50_800T	7	0.2	75.7	[12]
N-doped carbon (0.05 mg cm^{-2})	0.5 M H_2SO_4 0.1 M K_2SO_4	0.49 0.52	>90 90	[13]
Co–N–C	7.4	0.3-0.4	>60	[14]
O-CB (0.2 mg cm^{-2})	0.1 M Na_2SO_4	0.47	55	[15]
Boron doped carbon	0.1 M Na_2SO_4	0.35	80	[16]
Mesoporous nitrogen-doped carbon	1	0.1	>90	[17]
Mesoporous nitrogen doped carbon	0.5 M H_2SO_4	0.2	>90	[18]
Oxidized CNTs	0.1 M KOH 0.1 M PBS 0.1 M $HClO_4$	0.70 0.40 0.15	~90 ~85 ~50	[19]
Co–N–C	1	0.3	>40	[14]
Single site Co-N-C (0.1 mg cm^{-2})	0.1 M K_2SO_4 0.5 M H_2SO_4	0.71 0.83	55 80	[20]
F-doped carbon (0.86 mg cm^{-2})	0.05 M H_2SO_4	0.425	97.5	[21]
900-BNC (0.1 mg cm^{-2})	0.5 M K_2SO_4	0.35	~80	**This work**

Table S10. Comparison of H_2O_2 performance of different catalysts using different flow cells.

Material	Cell	pH	H_2O_2 Faradaic Efficiency (%)	H_2O_2 Production Rate (mmol cm^{-2} sec^{-1})	Reference
CoPc-CNT(O) CoPc-CNT CNT(O) (0.2 mg cm^{-2})	Flow Cell	1 M Na_2SO_4	92 90 90	1.43E-3 1.4E-3 9.3E-3	[22]
B-C (0.5 mg cm^{-2})	Flow Cell	1 M KOH	80	2.6E-4	[16]
N-doped carbon (0.2 mg cm^{-2})	Flow Cell	0.5 M Na_2SO_4 0.1 M KOH 0.5 H_2SO_4	70 59.5 34.3	1.37E-4 1.17E-4 6.7E-5	[23]
$OCNS_{900}$ (1 mg cm^{-2})	Flow Cell	0.1 M KOH	89.6	2.14E-6	[24]
900-BNC (0.5 mg cm^{-2})	Flow Cell	0.5 M K_2SO_4	78	2.4E-4	**This work**

Section S5. References

(1) Gill, T. M.; Zheng, X. Comparing Methods for Quantifying Electrochemically Accumulated H2O2. *Chemistry of Materials* **2020**, *32* (15), 6285-6294. DOI: 10.1021/acs.chemmater.0c02010.

(2) Chen, S.; Chen, Z.; Siahrostami, S.; Kim, T. R.; Nordlund, D.; Sokaras, D.; Nowak, S.; To, J. W. F.; Higgins, D.; Sinclair, R.; et al. Defective Carbon-Based Materials for the Electrochemical Synthesis of Hydrogen Peroxide. *ACS Sustainable Chemistry and Engineering* **2018**, *6* (1), 311-317. DOI: 10.1021/acssuschemeng.7b02517.

(3) Bruhwiler, P. A.; Maxwell, A.; Puglia, C.; Nilsson, A.; Andersson, S.; Martensson, N. pi * and sigma * Excitons in C 1s Absorption of Graphite. *Phys Rev Lett* **1995**, *74* (4), 614-617. DOI: 10.1103/PhysRevLett.74.614 From NLM Publisher.

(4) Schiros, T.; Nordlund, D.; Palova, L.; Zhao, L.; Levendorf, M.; Jaye, C.; Reichman, D.; Park, J.; Hybertsen, M.; Pasupathy, A. Atomistic Interrogation of B-N Co-dopant Structures and Their Electronic Effects in Graphene. *ACS Nano* **2016**, *10* (7), 6574-6584. DOI: 10.1021/acsnano.6b01318 From NLM PubMed-not-MEDLINE.

(5) Ding, J.; Wang, H. F.; Yang, X.; Ju, W.; Shen, K.; Chen, L.; Li, Y. A Janus heteroatom-doped carbon electrocatalyst for hydrazine oxidation. *National Science Review* **2022**, *10* (3). DOI: 10.1093/nsr/nwac231/6767723.

(6) Yu. V. Fedoseeva; M. L. Kosinova; S. A. Prokhorova; I. S. Merenkov; L. G. Bulusheva; A. V. Okotrub; Kuznetsov, F. A. X-ray spectroscopic study of the electronic structure of boron carbonitride films obtained by chemical vapor deposition on Co/Si and CoOx/Si substrates. *Journal of Structural Chemistry* **2012**, *53*, 690-698.

(7) Li, L.; Tang, C.; Zheng, Y.; Xia, B.; Zhou, X.; Xu, H.; Qiao, S. Z. Tailoring Selectivity of Electrochemical Hydrogen Peroxide Generation by Tunable Pyrrolic-Nitrogen-Carbon. *Advanced Energy Materials* **2020**, *10* (21). DOI: 10.1002/aenm.202000789.

(8) Chen, S.; Chen, Z.; Siahrostami, S.; Higgins, D.; Nordlund, D.; Sokaras, D.; Kim, T. R.; Liu, Y.; Yan, X.; Nilsson, E.; et al. Designing Boron Nitride Islands in Carbon Materials for Efficient Electrochemical Synthesis of Hydrogen Peroxide. *Journal of the American Chemical Society* **2018**, *140* (25), 7851-7859. DOI: 10.1021/jacs.8b02798.

(9) Mehta, S.; Gupta, D.; Nagaiah, T. C. Selective Electrochemical Production of Hydrogen Peroxide from Reduction of Oxygen on Mesoporous Nitrogen Containing Carbon. *ChemElectroChem* **2022**, *9* (2). DOI: 10.1002/celc.202101336.

(10) Liu, Y.; Quan, X.; Fan, X.; Wang, H.; Chen, S. High-yield electrosynthesis of hydrogen peroxide from oxygen reduction by hierarchically porous carbon. *Angewandte Chemie - International Edition* **2015**, *54* (23), 6837-6841. DOI: 10.1002/anie.201502396.

(11) Yamanaka, I.; Murayama, T. Neutral H2O2 synthesis by electrolysis of water and O2. *Angewandte Chemie - International Edition* **2008**, *47* (10), 1900-1902. DOI: 10.1002/anie.200704431.

(12) Sun, Y.; Sinev, I.; Ju, W.; Bergmann, A.; Dresp, S.; Kühl, S.; Spöri, C.; Schmies, H.; Wang, H.; Bernsmeier, D.; et al. Efficient Electrochemical Hydrogen Peroxide Production from Molecular Oxygen on Nitrogen-Doped Mesoporous Carbon Catalysts. *ACS Catalysis* **2018**, *8* (4), 2844-2856. DOI: 10.1021/acscatal.7b03464.

(13) Sun, Y.; Li, S.; Jovanov, Z. P.; Bernsmeier, D.; Wang, H.; Paul, B.; Wang, X.; Kühl, S.; Strasser, P. Structure, Activity, and Faradaic Efficiency of Nitrogen-Doped Porous Carbon Catalysts for Direct Electrochemical Hydrogen Peroxide Production. *ChemSusChem* **2018**, *11* (19), 3388-3395. DOI: 10.1002/cssc.201801583.

(14) Jung, E.; Shin, H.; Lee, B. H.; Efremov, V.; Lee, S.; Lee, H. S.; Kim, J.; Hooch Antink, W.; Park, S.; Lee, K. S.; et al. Atomic-level tuning of Co-N-C catalyst for high-performance electrochemical H(2)O(2) production. *Nat Mater* **2020**, *19* (4), 436-442. DOI: 10.1038/s41563-019-0571-5 From NLM PubMed-not-MEDLINE.

(15) Zhang, H.; Li, Y.; Zhao, Y.; Li, G.; Zhang, F. Carbon Black Oxidized by Air Calcination for Enhanced H2O2 Generation and Effective Organics Degradation. *ACS Appl Mater Interfaces* **2019**, *11* (31), 27846-27853. DOI: 10.1021/acsami.9b07765 From NLM PubMed-not-MEDLINE.

(16) Xia, Y.; Zhao, X.; Xia, C.; Wu, Z. Y.; Zhu, P.; Kim, J. Y. T.; Bai, X.; Gao, G.; Hu, Y.; Zhong, J.; et al. Highly active and selective oxygen reduction to H2O2 on boron-doped carbon for high production rates. *Nat Commun* **2021**, *12* (1), 4225. DOI: 10.1038/s41467-021-24329-9 From NLM PubMed-not-MEDLINE.
(17) Fellinger, T. P.; Hasché, F.; Strasser, P.; Antonietti, M. Mesoporous nitrogen-doped carbon for the electrocatalytic synthesis of hydrogen peroxide. *Journal of the American Chemical Society* **2012**, *134* (9), 4072-4075. DOI: 10.1021/ja300038p.
(18) Park, J.; Nabae, Y.; Hayakawa, T.; Kakimoto, M. A. Highly selective two-electron oxygen reduction catalyzed by mesoporous nitrogen-doped carbon. *ACS Catalysis* **2014**, *4* (10), 3749-3754. DOI: 10.1021/cs5008206.
(19) Lu, Z.; Chen, G.; Siahrostami, S.; Chen, Z.; Liu, K.; Xie, J.; Liao, L.; Wu, T.; Lin, D.; Liu, Y.; et al. High-efficiency oxygen reduction to hydrogen peroxide catalysed by oxidized carbon materials. *Nature Catalysis* **2018**, *1* (2), 156-162. DOI: 10.1038/s41929-017-0017-x.
(20) Sun, Y.; Silvioli, L.; Sahraie, N. R.; Ju, W.; Li, J.; Zitolo, A.; Li, S.; Bagger, A.; Arnarson, L.; Wang, X.; et al. Activity-Selectivity Trends in the Electrochemical Production of Hydrogen Peroxide over Single-Site Metal-Nitrogen-Carbon Catalysts. *Journal of the American Chemical Society* **2019**, *141* (31), 12372-12381. DOI: 10.1021/jacs.9b05576.
(21) Zhao, K.; Su, Y.; Quan, X.; Liu, Y.; Chen, S.; Yu, H. Enhanced H2O2 production by selective electrochemical reduction of O2 on fluorine-doped hierarchically porous carbon. *Journal of Catalysis* **2018**, *357*, 118-126. DOI: 10.1016/j.jcat.2017.11.008.
(22) Lee, B.-H.; Shin, H.; Rasouli, A. S.; Choubisa, H.; Ou, P.; Dorakhan, R.; Grigioni, I.; Lee, G.; Shirzadi, E.; Miao, R. K.; et al. Supramolecular tuning of supported metal phthalocyanine catalysts for hydrogen peroxide electrosynthesis. *Nature Catalysis* **2023**. DOI: 10.1038/s41929-023-00924-5.
(23) Bao, Z.; Zhao, J.; Zhang, S.; Ding, L.; Peng, X.; Wang, G.; Zhao, Z.; Zhong, X.; Yao, Z.; Wang, J. Synergistic effect of doped nitrogen and oxygen-containing functional groups on electrochemical synthesis of hydrogen peroxide. *Journal of Materials Chemistry A* **2022**, *10* (9), 4749-4757. DOI: 10.1039/d1ta09915a.
(24) Chen, S.; Luo, T.; Chen, K.; Lin, Y.; Fu, J.; Liu, K.; Cai, C.; Wang, Q.; Li, H.; Li, X.; et al. Chemical Identification of Catalytically Active Sites on Oxygen-doped Carbon Nanosheet to Decipher the High Activity for Electro-synthesis Hydrogen Peroxide. *Angew Chem Int Ed Engl* **2021**, *60* (30), 16607-16614. DOI: 10.1002/anie.202104480 From NLM PubMed-not-MEDLINE.